

# Neutron Skin Measurement of Tin Isotopes



*Dominika Glowa*

Third Year Report  
June 2014

# Abstract

Heavy atomic nuclei are thought to have proton and neutron radial distributions which have different sizes. This difference is usually quantified in terms of a neutron skin ( $r_{np}$ ), defined as the difference between the root mean square radii of the neutrons and proton distributions ( $r_{np} = r_n^2 - r_p^2$ ). The nature or even existence of the neutron skin is currently not well established. Different nuclear theories give different predictions for the neutron skin thickness of a typical heavy nucleus ranging from 0.05 to 0.35 fm. Accurate measurement of the properties of the neutron skin would be a powerful constraint to differentiate between models of nuclear structure and improve our knowledge of the basic Equation Of State (EOS) for neutron rich matter. Particularly, the rate at which the neutron skin thickness changes across an isotopic chain of nuclei gives a tight constraint on the EOS and is also amenable to experimental determination with small systematic error. Improving our knowledge of the EOS for neutron rich matter is a crucial step to a deeper understanding of nuclear structure and compact astrophysical objects such as neutron stars. This thesis describes the first measurement of neutron skin through the study of pions coherent photoproduction from nuclei along an isotopic chain of tin.

This experiment was carried out in the A2 hall of the MAMI facility in Mainz, Germany in October 2012. The incident photon beam comprised energy tagged photons in the range of  $E_\gamma=150\text{-}800$  MeV with an intensity of  $10^8 \text{ sec}^{-1}$ . Experimental data was obtained for three different tin targets,  $Sn^{116}$ ,  $Sn^{120}$  and  $Sn^{124}$ . The products from the resulting photoreactions were measured in the Crystal Ball detector and in the TAPS calorimeter systems, with track and particle identification information for charged particles provided by a multi wire proportional chamber (MWPC) and a particle identification detector (PID).

The experiment provides the first information on the evolution of the neutron

---

skin thickness along an isotopic chain using an electromagnetic probe. The results are compared with a range of theoretical models and previous data from strongly interacting probes. The new data provides an important experimental constraint on the basic properties of the EOS in atomic nuclei.

# Chapter 1

## Experimental details

### 1.1 Overview

The experiment has been performed in the A2 hall of MAMI facility at the Johannes Gutenberg Universitaet in Mainz, Germany in October 2012 over the course of 21 days.

The key element of the MAMI installation is the Mainzer Mikrotron; it provides a 100% duty factor electron beam that can be directed to any one of the four experimental halls. The photon beam utilized in the experiment was produced by directing the electron beam onto a thin metallic radiator creating bremsstrahlung radiation. The Glasgow Photon Tagger momentum analyses the recoiling electrons from the bremsstrahlung process and provides information on the energy of the photons. The tagger comprises a large dipole electromagnet and a highly segmented detector apparatus near the focal plane of the magnet. The tin target, located in the center of the Crystal Ball (CB), has been exposed to the bremsstrahlung photon flux and the products of resulting photoreactions have been detected in the CB and TAPS segmented detectors. Since neutral pions have a very short lifetime, order of  $10^{-18}$ s it is not possible to detect them directly. Instead, the products of their dominant decay, two gamma photons, are detected in the apparatus and the pion's 4 momentum is reconstructed from this information. A schematic picture of the MAMI facility is presented In Fig. 1.1.

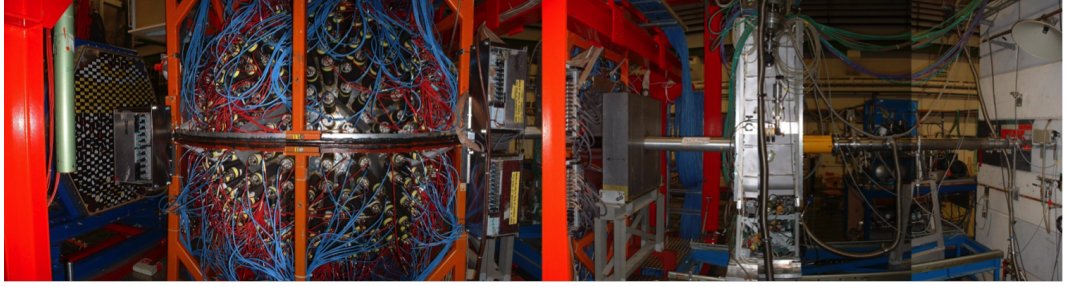


Figure 1.1: A diagram illustrating the experiential setup in A2 hall at MAMI.

In addition to the CB and TAPS detectors, the Edinburgh Particle Identification Detector (PID), providing information about charged particles detected in CB, and Multi Wire Proportional Chambers (MWPC), providing identification of charged particles and tracking information, have been used. The details of all detectors as well as the MAMI facility itself are presented in the following sections.

## 1.2 Mainzer Mikrotron

The Mainz Microtron (MAMI) is a continuous wave electron accelerator. It is located at the Institut fuer Kernphysik at Johannes Gutenberg Universitaet in Mainz, Germany. MAMI operates since 1979 and in the interim period has been upgraded three times, achieving succesively higher electron beam energies and intensities. The most recent upgrade, to MAMI-C, provides an electron beam energy up to 1.6GeV with a helicity polarization degree of 80% and a beam current of over  $20\mu\text{A}$  (unpolarized electron beams of up to  $100\mu\text{A}$  can be produced).

The MAMI facility operates using a racetrack microtron design. In this a beam of electrons is accelerated by a series of radio frequency LINAC (linear accelerator) sections and recirculated through the LINACs using a magnetic field. Each time the beam passes through the LINAC its orbit through the magnetic field changes, with higher energy electrons taking wider paths through the magnetic field. These paths are finely tuned such that the electrons always pass through the linac in time with the radiofrequency (rf) electric field frequency applied to the LINACs. The design of the early stages of the MAMI RTM employ two homogeneous semicircular magnets and a small linear accelerator (LINAC) placed between

them (Fig. 1.2). Repeated passes through LINAC ensure that high beam energy can be achieved even if the acceleration with each pass is relatively small. The first microtron has been constructed at the National Research Council of Canada in 1947, according to the design of V. I. Veksler, where the electrons, accelerated along circular paths, reached energies of up to 4.6 MeV [4]. Ever since that first design the idea of a microtron has been worked upon to reach higher electron energies. The concept of a racetrack microtron (RTM) has been proposed already in 1945 but the first RTM was constructed only in 1961 and provided electron beams of energies up to 12 MeV.

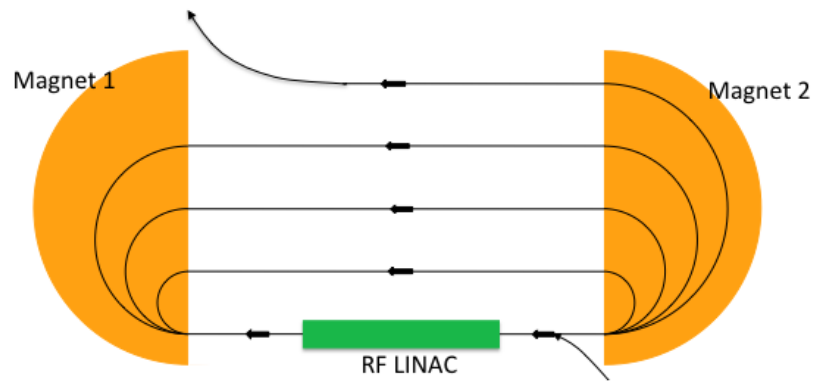


Figure 1.2: Schematics of a simple microtron.

In 1979 a RTM was first used successfully at MAMI facility, producing an electron beam of 14 MeV (MAMI-A1). Subsequent upgrade (MAMI-A2) introduced another RTM to the design and allowed for beam energies up to 180 MeV in 1983. The need for even higher beam energies inspired yet another upgrade (MAMI B), and in 1990 with the addition of another RTM it was possible to achieve energies of up to 855 MeV. However, quickly advancing research in the fields of nuclear and particle physics required even higher energies. The design allowing for beam energies of 1.5 GeV however, could not employ another RTM based on the dipole magnet design; the magnets required for achieving such energies would have to weigh 2500 tons each which was neither financially nor spatially feasible; for comparison, magnets in the MAMI B design weigh only 450 tons. The issue has been bypassed by adding a harmonic double-sided microtron (HDSM). In this concept, rather than using two magnets bending the beam by 180°, four 90° and two accelerating sections have been used (Fig. 1.3).

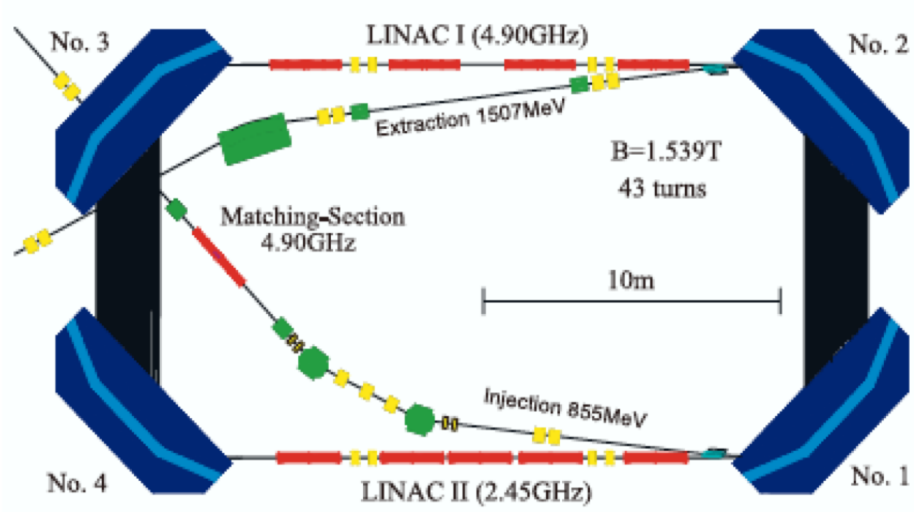


Figure 1.3: Schematic picture of a harmonic double-sided microtron for MAMI C.

This design allowed for the production of a 1.508GeV electron beam in December 2006, and energy as high as 1.604GeV has been reached in 2009.

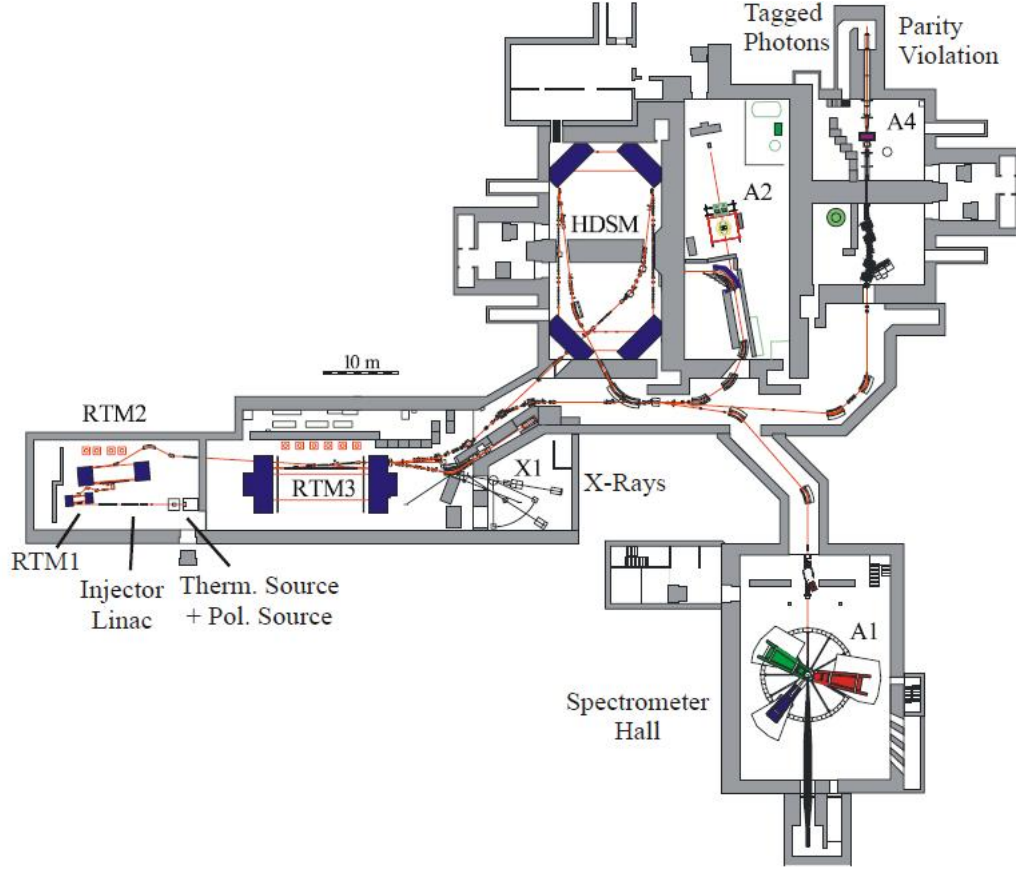


Figure 1.4: Floor plan of the MAMI facility.

### 1.3 Glasgow Photon Tagger

The experiment has been performed in the A2 hall of MAMI (Fig .1.4), which houses the installation dedicated to the studies of reactions between high-energy photons with atomic nuclei. The photon beam used in this experiment has been produced when the electrons ejected from RTM3 were directed into A2 hall and incident onto a thin,  $10\mu\text{m}$  thick, copper radiator. The 855MeV electrons can interact in the electrostatic field of the copper nuclei and radiate photons; the energy of these bremsstrahlung photons can be calculated from:

$$E_\gamma = E_0 - E_e \quad (1.1)$$

where  $E_0$  is the initial beam energy and  $E_e$  is the energy of the scattered



electrons. This equation neglects the energy loss to the recoiling copper nuclei, however, the mass of the copper nucleus is high enough to assume that only negligible amount of kinetic energy has been transferred.

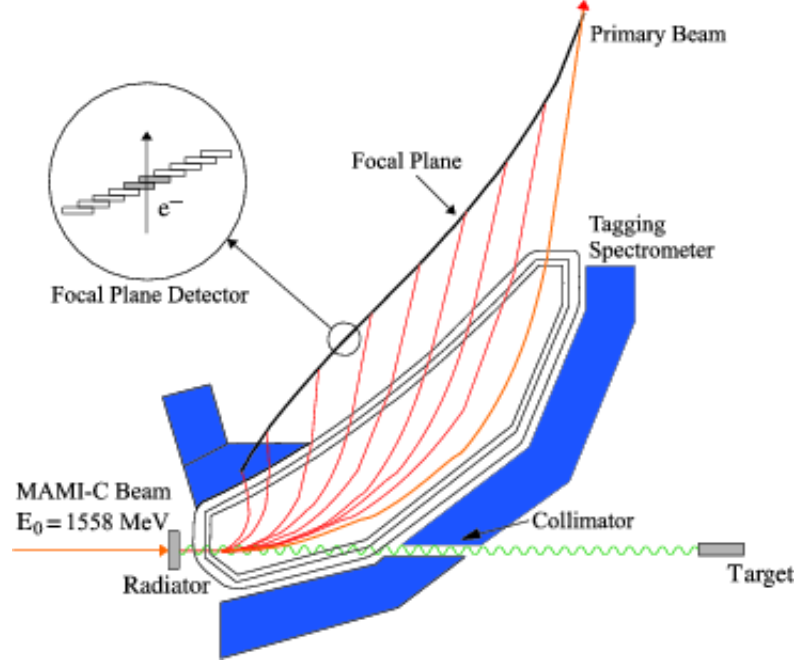


Figure 1.5: Schematic picture of the Glasgow Photon Tagger [23].

The Glasgow Photon Tagger (GPT) is a large momentum acceptance spectrometer. Electrons, after passing through radiator, first enter the magnetic field of a quadrupole magnet, which focuses them vertically, and then the dipole magnet disperses them horizontally according to their energy. For example, the lower energy electrons associated with the production of higher energy photons are bent more significantly by the field compared to the higher energy electrons. The momentum of the bremsstrahlung electrons is analysed in the Glasgow Photon Tagger (Fig. 1.5). By identifying the path of the electron in the field and correlating the timing of the electron with the subsequent photuclear reaction in the target then the photons can be characterised event-by-event. This is referred to as a tagged photon beam. Electrons that have radiated bremsstrahlung photons are directed onto a segmented focal plane detector. The electrons that haven't radiated any photons follow a curved path into a beam dump.

iiiiii HEAD The focal plane (FP) detector consists of 353 wrapped

in a double-sided, aluminized Mylar plastic scintillators [12]. Each of these scintillators is 80mm long and 2mm thick with a varying width of 9-32 mm. The width decreases along the focal plane in order to keep the energy resolution constant. The scintillators overlap by more than half-width (Fig 3.2) what allows for electron detection by coincidence signals in two adjacent detectors with the energy resolution of 2-8MeV, with the average of 4MeV, depending on the beam energy [13]; the coincidence condition also allows for significant reduction of the low energy background in the detector. ===== The focal plane (FP) detector consists of 353 plastic scintillator detectors wrapped in a double-sided, aluminized Mylar [?]. Each of these scintillators is 80mm long and 2mm thick with a varying width of 9-32 mm. The detector width decreases along the focal plane in order to keep the energy resolution constant. The scintillators overlap by more than a half-width (Fig 3.2) which allows for electron detection by coincident signals in two adjacent detectors. The size of this overlap fixes the achievable energy resolution, which ranges from 2-8MeV with an average of 4MeV, depending on the beam energy [13]; the coincidence condition also allows for significant reduction of the low energy background in the detector. 05b600032413a648185c176c02b19650e9302a8f

Each scintillator is connected to an R1635 Hamamatsu photomultiplier tube (PMT), which are shielded from the magnetic field by 0.7mm thick steel plates and an individual sheath of  $\mu$ -metal. The high segmentation of the array allows for the tagging of high-flux photon beams. When used with the 1.508GeV electron beam, the tagger operate at a rate of up to  $10^8 \text{ s}^{-1}$  flux photons in the energy range of 0.08-1.401GeV. The maximum rate is determined by the operating limit of the individual PMTs being 1MHz per channel to avoid unnecessary reduction in their operating lifetime. The bremsstrahlung photons pass the magnetic field of the GPT unaffected and exit into the experimental hall through a channel bored into the dipole magnet.

In order to ensure the small size of the beam spot on the target a 3mm collimator is employed near to the exit of this bored channel. Employing a collimator produces a more well defined beam spot on the target, but also reduces the photon flux. Without collimation, the photon flux incident upon the target would be related more directly to the number of hits in the FP detector. To determine the exact luminosity of the photon beam, tagging

efficiency measurements have to be made where a 100% efficient lead glass detector is placed in the beamline. This efficiency correction is applied individually to each detector channel in the focal-plane detector, as the efficiency depends on the opening angle of the gamma beam, which depends on the gamma (or electron) energy. The tagging efficiency is defined as:

$$\epsilon_{tagg} = \frac{N_\gamma}{N_e} \quad (1.2)$$

where  $N_\gamma$  is the number of photons passing through the collimator and registered by the lead glass detector, and  $N_e$  is the number of hits in the FP detector. During the tagging efficiency measurement, carried out as separate runs during the experiment, a lead glass detector is placed in the path of the collimated beam. The beam intensity employed in this measurement is lower than that used in the actual experiment in order to protect the lead glass detector from the potential radiation damage and to reduce the number of multiple hits in the FP detector.

## 1.4 Crystal Ball

The Crystal Ball (CB) has been constructed and used in various experiments long before being installed at MAMI. First used in 1970s for the colliding beam experiments at the SLAC facility to obtain first accurate measurements of  $\frac{J}{\psi}$  [10]. Later it has been used at DESY and in Brookhaven National Laboratory and arrived in its current home, the A2 hall at MAMI only in 2002. The CB is a highly segmented calorimeter, it consists of 672 sodium iodide (NaI) crystals, each in a shape of truncated triangular pyramid, and arranged into a shape of a 20 sided polyhedron (Fig. 1.6).

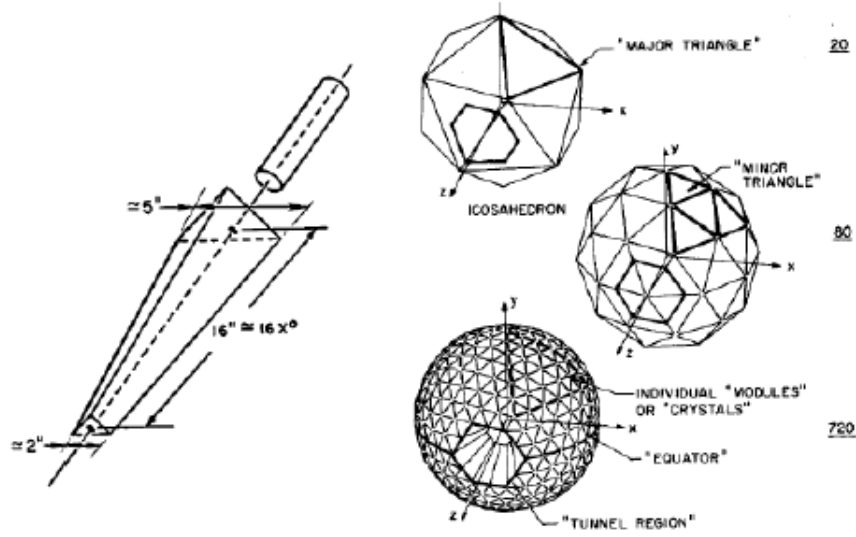


Figure 1.6: NaI crystal and CB geometry [24].

Having been designed for the colliding beam experiments, the plan had to accommodate the beamline running across and through the center of the CB. Because of that the section corresponding to 24 crystals on opposite poles of the sphere has been cleared making room for the beamline components. The remaining crystals have been grouped into two, hermetically sealed hemispheres; the isolation of the crystals from the outside environment was essential because NaI is highly hygroscopic and degenerates when exposed to the air moisture.

The outer and inner radii of the CB are 66cm and 25.3cm respectively. The two hemispheres are enclosed within a 1.5mm thick steel casing and the width of the gap between them, the equator region, is 0.8cm thick and consists of two 1.6mm thick steel plates and an adjustable air gap, usually set to 5mm. Such design allows for the coverage close to complete angular range, 94% of  $4\pi$ .

The of the 20 faces (major triangle) of the CB polyhedron is segmented into 4 smaller triangles (minor triangle) which are in turn divided into 9 segments corresponding to individual NaI crystals (Fig. 1.6). Each crystal, 40.6cm long with the sides of the inner and outer faces being 5.1cm and 12.7cm respectively, is optically shielded with a reflector paper and aluminized Mylar, and connected to the 5.1cm diameter SRC L50 B01 PMT, chosen for a good linear response over

a wide range of energies. These are mounted outside the CB and scintillation light is fed into them through a 5cm air gap and a thick glass window, separating the NaI crystals from the PMTs. This set up constitutes part of the hermetic design helping to maintain isolated environment for the sodium iodide crystals. During the experiment photons produced in the reactions inside the CB trigger an electromagnetic shower which deposits energy in the NaI crystals, chosen for their good energy resolution across a wide range of energies. The amount of deposited energy and the number of crystals hit depend on the reaction studied; the information about the nature of the particles detected in the CB are recovered from the analysis of the hits in the NaI clusters; the basic detection properties of the CB are summarized in the below table [5].

Table 1.1: Crystal Ball Detection Parameters		
Energy Photon Resolution		
	$\frac{\sigma}{E}$	$\frac{1.7\%}{E(GeV^{0.4})}$
Angular Resolution	azimuthal:	$\frac{2^\circ}{\sin\theta}$
	polar:	$2-3^\circ$
Angular Coverage	azimuthal:	0 - 360°
	polar:	20 - 160°
Time resolution		
		$\sigma \ 2ns$

## 1.5 Multi Wire Proportional Chambers

Inside the tunnel region inside the Crystal Ball another detector by the name of Multi Wire Proportional Chambers (MWPCs) is located. They are tasked with retrieving information about charged particles; the design is that of the one originally used in DAPHNE [6].

Each of the two MWPCs is built up of three layers; internal and external stripes acting as cathodes and the middle layer of wires the anode (Fig. 1.7). The cylindrical cathodes are made from the 1mm thick rohacell laminated with aluminum stripes, 4mm wide and 0.1um thick, spaced 0.5mm apart. The stripes are wound helically at 45° with respect to the anode wires, in opposite directions.

The anode is made up of  $20\mu\text{m}$  Tungsten wires 2mm apart and parallel to the beam direction. The chambers are filled with a gas mixture of argon(79.5%), ethane (30%) and freon (0.5%).

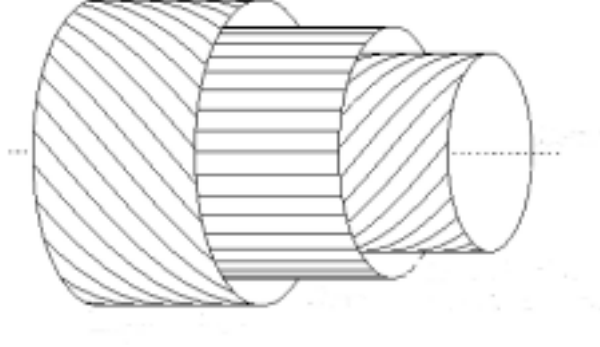


Figure 1.7: Diagram of MWPC showing the positions of anode wires and cathodes stripes [1].

Correlating the hits in both cathode stripes and the anode wires does the determination of the tracks of charged particles. In the case of neutral particles experiments the information provided by the MWPCs is used to determine the position of the target inside the CB. This information is extracted from the linear fit to the polar angle and z-position of the hits registered in both chambers to obtain the azimuthal and theta and angles for each track. Then the trajectories of multiple tracks are analyzed to find their intersection, and therefore obtain the position of the target. The design of the chambers allows this detector for full 360deg coverage of the azimuthal angle and the theta range between  $21^\circ$  and  $159^\circ$ ; the specifics of the chambers are summarized in the below table.

Table 3.4.1 MWPCs design parameters.

## 1.6 Particle Identification Detector

The Edinburgh Particle Identification Detector (PID) is located inside the Crystal Ball and surrounded by the MWPCs. It is a  $\frac{dE}{dx}$  detector and together with the CB, it provides information about the charged particles.

PID consists of 24 EJ204 plastic scintillators arranged in the cylindrical shape. Each scintillator strip is 500mm long and 4mm thick, and in order to minimize

gaps between the adjacent scintillators the design demanded they have right-angle trapezium cross-section. Each strip is wrapped in the aluminized Mylar foil to optically isolate scintillation light. The scintillators are connected to the Hamamatsu R1635 and E1761-04 PMTs via perspex light guides. An aluminum ring with 24 holes, where the PMTs are positioned so to match the arrangement of the scintillator strips, supports the construction (Fig. 1.8). The entire detector is wrapped in the black Tedlar foil to ensure it is lightproof.

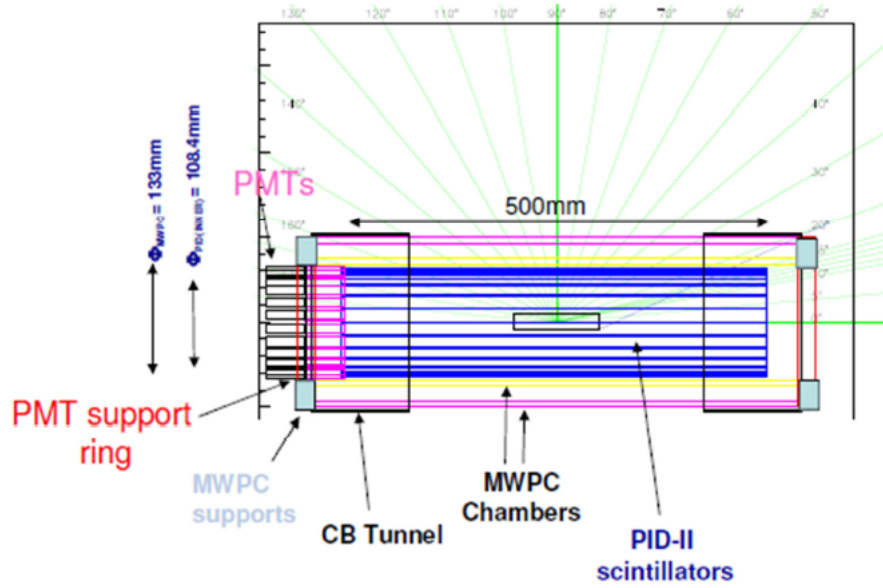


Figure 1.8: PID schematics.

===== HEAD The design of allows PID for the full coverage of azimuthal angle and 20° to 160° coverage of the polar angle, what matches exactly the parameters of the CB. When a charged particle passes through the scintillator it deposits there a fraction of its energy and the rest of its energy is detected in the Crystal Ball. The identity of such particle is determined by correlating the events from both detectors while enforcing that the hit in the CB is within 15° of the center of the PID scintillator (azimuthal angle). When plotting energy deposited in PID against energy registered in the CB on a two-dimensional plot a characteristic banana shape is obtained (Fig. 1.9). The proton and pion loci are easily identifiable from such a plot. ===== The design of allows PID for the full coverage of azimuthal angle and 20° to 160° coverage of the polar

angle, what matches exactly the parameters of the CB. When a charged particle passes through the scintillator it deposits there a fraction of its energy and the rest of its energy is detected in the Crystal Ball. The identity of such particle is determined by correlating the events from both detectors while enforcing that the hit in the CB is within 15o of the center of the PID scintillator (azimuthal angle). When plotting energy deposited in PID against energy registered in the CB on a two-dimensional plot a characteristic banana shape is obtained (Fig. 1.9). The proton and pion loci are easily identifiable from such a plot. [iiiii05b600032413a648185c176c02b19650e9302a8f](#)

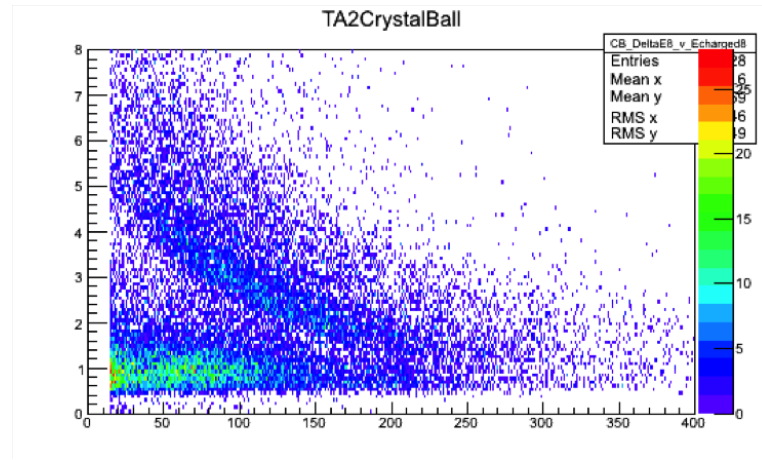


Figure 1.9:  $\Delta E$ -E plots of PID and CB energy deposits.

## 1.7 TAPS

Because Crystal Ball has been designed for the colliding beam experiments the detector doesn't cover 20o polar angle range in backward and forward directions, another detector had to be added to the system to make up for it. In MAMI, the CB is used for the fixed target experiments, where the reaction products are Lorentz boosted forward, and because of that an additional TAPS detector covering those missing forward 20 degrees has been mounted [18].

TAPS is located 1.5m downstream from the reaction vertex. It is a segmented calorimeter detector made from 385 hexagonal BaF<sub>2</sub> crystals (Fig. 1.10). Each crystal is 25cm long, wrapped in 8 layers of 38um thick UV-reflecting PTFE (Teflon) foil and a single layer of 15um thick aluminum foil for light proofing.



The cylindrical end part of each crystal is connected to the Hamamatsu R2059 PMT with silicone glue.

The barium fluoride crystals, even though have much lower scintillation output than NaI crystals used in CB, they have higher density ( $4.89\text{g/cm}^3$ ) and larger atomic number, and therefore provide just as good detection efficiency. The most important deciding factor for choosing BaF<sub>2</sub> crystals over other materials is its fast timing resolution ( $0.6\text{ns}$ ), which makes the detector ideal for identifying particles via time of flight (TOF) methods [18].

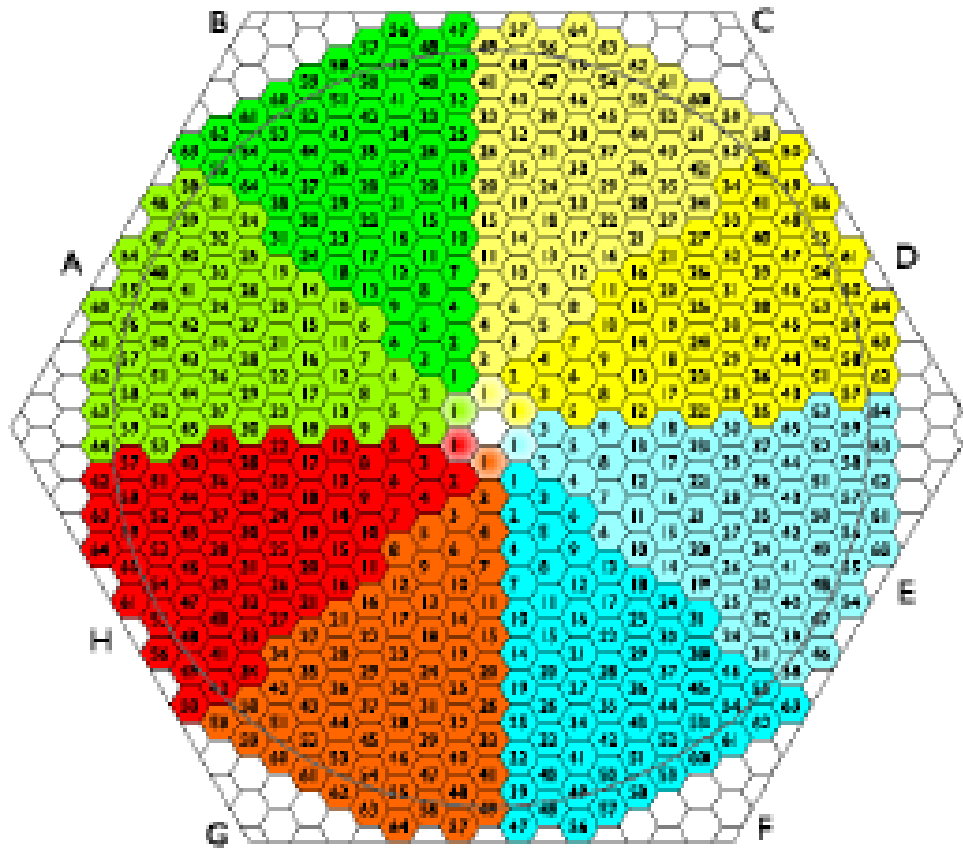


Figure 1.10: Diagram of the BaF<sub>2</sub> crystals arrangement in TAPS. Different colours represent sectors that can be defined in the trigger if required.

Directly in front of TAPS, there is an array of 5mm thick NE102A plastic scintillators the TAPS Veto detector. The output from this detector is collected

by the optic fibers in Valvo XP2972 phototubes. This addition to TAPS allows for distinguishing neutral and charged particles by correlating events from TAPS Veto and TAPS, and therefore makes the charged particles identification via  $\Delta E$ -E technique possible.

Another method used by TAPS to identify particles is time of flight technique. By measuring the time a particle traveled from the target to TAPS allows for distinguishing between slower protons and neutrons and particles traveling at or almost at the speed of light like photons and electrons.

A different method of particle identification, the pulse shape analysis, exploits the fact that BaF2 crystals have fast ( 0.6ns) and slow ( 620ns) decaying components. Each particle type leaves its own particular imprint on slow and fast components and by comparing the ratios of energy deposited in both, it is possible to tell different particles apart.

## 1.8 Targets

A previously performed experiment of the coherent  $\pi^0$  photoproduction on  $^{208}\text{Pb}$  target confirmed the existence of the neutron skin. However, in order to confirm the conclusions of that measurement it was desirable to repeat the experiment for another heavy nuclei. Furthermore, it has been shown that repeated measurements along isotopic chain promise better results to put tighter constraints on the parameters of the neutron rich matter equation of state [9].

The targets used in this experiment were three isotopes of tin ( $^{116}\text{Sn}$ ,  $^{120}\text{Sn}$  and  $^{124}\text{Sn}$ ); chosen because of its stability, and the elements' easy of availability. Theoretical calculations predict a change of 0.05 to 0.15fm in the neutron skin thickness when going across the isotopic chain of tin from  $^{116}\text{Sn}$  to  $^{124}$  (Fig. 1.11) [8]. Measuring the skin thickness across the isotopic chain cancels out any systematic error, and therefore, allows to accurately measure the changes predicted by the models.

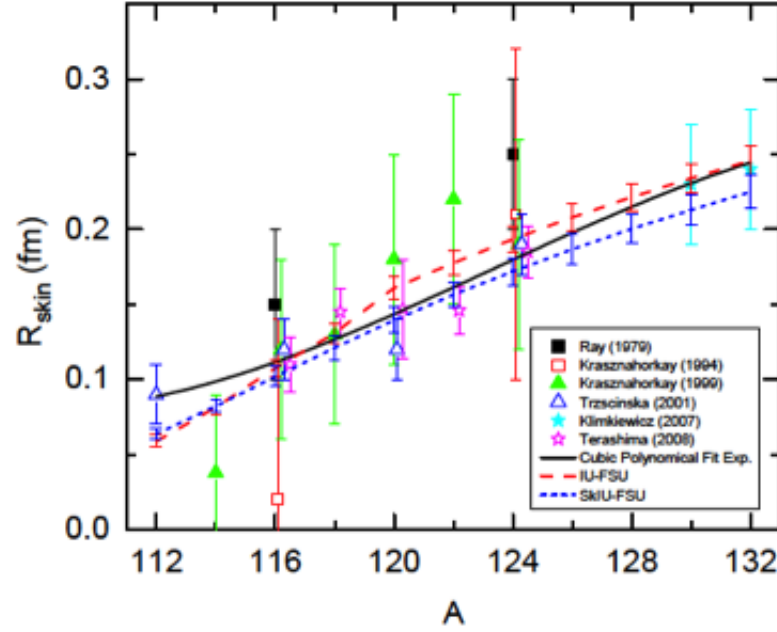


Figure 1.11: Predictions of neutron skin thickness for tin isotopes from the IU-FSU and SkIU-FSU models.

The targets were secured in a target holder by tape and placed inside a PVC tube at the centre of detectors. The details of the targets are given in the below table.

//Table 3.7 Tin targets. - will add later when I find where it is T.T

## 1.9 Data Acquisition

The analogue output signal of the detectors' PMTS has been read out and translated into a digital signal by the data acquisition system (DAQ) with the use of charge to digital converters (QDCs), analogue to digital converters (ADCs) and time to digital converters (TDCs). The latter measures the time difference between the start signal of an experimental trigger and the stop signal from a given detector element, thus provided the information about the time of the event. The ADCs give digital information proportional to the pulse height of the signal, while QDCs return digital signal proportional to charge; both these values, pulse height and charge are proportional to the energy deposited in the

detector element.

### 1.9.1 Tagger Electronics

The energy of the bremsstrahlung photons was obtained from the hit position of the recoiling electron on the tagger focal plane. The timing of such hit was used to match the events in the detectors with the hits on the focal plane. Providing that the a signal from the focal plane passed the threshold of the discriminator, a logic pulse was fed to a Compass Accumulation, Transfer and Control Hardware (CATCH) TDC (section 3.8.2) to record the time of the hit. Simultaneously, a signal from the discriminator was sent to FASTBUS scalars, which provided the count rate for each FP detector element. This was subsequently used to determine the photon flux.

### 1.9.2 Crystal Ball Electronics

As depicted in (Fig. 1.12), signals from each PMT are sent to fan-out units splitting the analogue output into three signals. One passes to a Flash ADC (F-ADC) via a delay, second goes through the discriminator and branches to a scalar and CATCH TDS. And the third signal is fed to the triggering electronics.

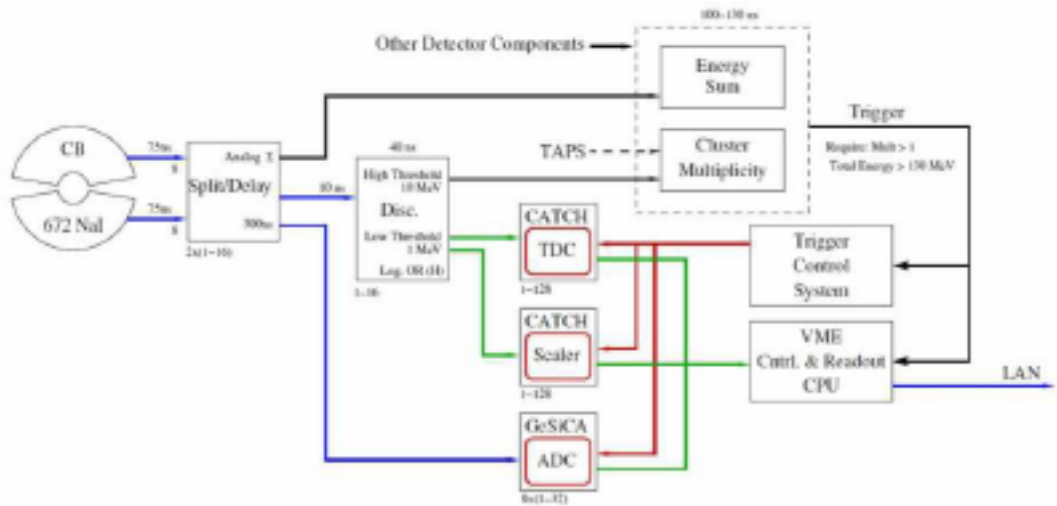


Figure 1.12: Crystal Ball electronics [15].

The integral of the pulse from each PMT was obtained from the F-ADCs, which sampled the shape of the signal with a frequency of 40 MHz. Since the DAQ was not prepared to handle such large volumes of data, only the integrals of pulses over three regions were taken. The integration is done over a time window of 750ns (30 signals). The first window was set to sample the pedestal whose signal is a convolution of remnant light and residual charge in the PMTs. The second window was set over the signal, and the third was set to evaluate the tail of the pulse. This set up allowed for the simultaneous measurement of the signal and the pedestal for every event, and with the dynamic subtraction of the pedestal from the signal, the energy resolution of the crystals could have been significantly improved.

Contrary to the typical TDCs, which are started by a hit in a relevant detector and stopped by a logic pulse from the trigger, CATCH TDCs, developed for the Compass experiment at CERN, allow for multiple hits in TDCs [7]. Using a 10GHz oscillator each TDC is running independently while the CERN-standard trigger control system synchronizes the signals in those TDCs. One of the TDCs is designated as a reference element and attached to the trigger. When an event passes the trigger threshold a logic pulse is sent to this reference TDC and the oscillator value is stored. When other TDCs record a hit, corresponding oscillator value is stored in a buffer. In order to extract the information on the timing of an event the oscillator value stored in the reference TDC has to be subtracted from the oscillator values recorded by other TDCs, the conversion rate of 117 ps/channel is then used [20].

### 1.9.3 TAPS Electronics

The signals from the TAPSPMTs received similar treatment to those from Crystal Ball and were also split into three separate signals. One signal was directed to a TDC via a constant fraction discriminator (CFD), which analyzed the shape of the pulse and provided accurate timing information for the QDCs. The other two signals were fed to separate QDCs, one with integration time of 40ps, other with 200ps, this double integration allows for a pulse shape analysis.

### 1.9.4 Triggering Electronics

While the event is being registered by DAQ, no other event is being recorded; this is defined as dead time. In order to reduce the effects of the dead time, a series of triggers were set up to limit the events read by DAQ only to those relevant to the experiment. Two LeCroy LRS 4805 logic units were used to define the conditions an event must satisfy in order to be recorded.

The first level trigger for this experiment required the sum of energy deposited in all 672 NaI crystals to be greater than 40 MeV. For the second level trigger, DAQ grouped NAI crystal into clusters of 16, and it was required that there were two hit clusters detected in the CB. When those two conditions were satisfied DAQ read the event and reset the electronics.

## 1.10 Analysis code

Online analysis and monitoring of the data have been done using the AcquRoot framework. AcquRoot has been written in C++ specifically for the data analysis at MAMI, it uses libraries and tools of ROOT [2, 3]. AcquRoot consists of three components, AcquDAQ Data Acquisition, AcquRoot Analysis and AcquMC Event Generator.

Offline analysis was done with a2GoAT (Generation of Analysis Trees). In this framework AcquRoot is used to produce analysis trees containing only basic track information. GoAT software package is used to process those trees; here particle reconstruction, all the data checks and sorting is performed.

# Chapter 2

## Calibrations

This chapter addresses the calibrations of all the detectors. The process involved converting raw signals from the detectors into real physical quantities allowing for the energy, position and timing corrections to be determined and applied in the subsequent analysis.

### 2.1 Tagger Energy Calibrations

The tagger energy calibration determines the relation between tagger channel number and electron energy. The calibrations were carried out by the colleagues at the University of Glasgow [13].

In order to make a tagger energy calibration, an incident MAMI electron beam of an energy of interest is bent in the magnetic field; for a 855MeV beam, field of 1.025T is used. Then the magnetic field was varied in small steps to guide the beam through the focal plane and an energy measurement was taken at each step. Six different electron beam energies were used for the calibration, they ranged from 195.22MeV to 705.26 MeV, with the uncertainty of 0.16MeV; the uncertainty in the magnetic field was 0.01mT [17].

The varying magnetic field required to sweep the beam across a given channel allowed for the determination of a position of a hit in a FP detector with an accuracy of 0.05 channel width. Finally, in order to relate the the FP channel number to the electron energy a linear interpolation between different energies was used.

## 2.2 Crystal Ball Calibrations

### 2.2.1 Clustering Algorithm

Photons entering Crystal Ball deposit their energy in the NaI crystals via electromagnetic showers which hit multiple crystals in each event. These groups of hit crystals are called clusters. The accurate analysis of the CB events required an algorithm which identifies the clusters and recovers information about the incident photon's energy and position from the energy deposited in the crystals within a cluster.

First step in the analysis is to identify a crystal with the highest energy deposit, central crystal of the cluster, and it's 12 closest neighbours (Fig. 2.1). A hit in this central crystal provides the timing information for the event. The energies of the neighbouring crystals are scanned and if their energies are greater than the threshold energy of around 2MeV they are added to the cluster. Only 12 closest neighbours of the central crystal are considered in the algorithm because it has been confirmed that in 98% of the cases the energy deposit of the shower triggers only 13 crystals [21]. Then the total energy of the cluster is obtained as:

$$E_{sum} = \sum_k E_i \quad (2.1)$$

where,  $E_i$  is the energy of the  $i$ th crystal in the cluster of  $k$  detector elements. Then the condition of the the total energy of the cluster being greater than 20MeV is applied to suppress the effects of the background.

The position of the hit is calculated as the weighted mean position given by the below equation:

$$r_{mean} = \frac{\sum_k \sqrt{E_i} r_i}{\sum_k \sqrt{E_i}} \quad (2.2)$$

where,  $E_i$  is the energy deposited in the  $i$ th crystal and  $r_i$  is the position of the  $i$ th crystal in the cluster.



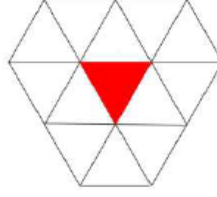


Figure 2.1: Schematic representation of a NaI cluster. The central triangle, shaded in red, depicts a triangular face of the NaI crystal and is the logical centre of the cluster. The other 12 triangles are its closest neighbours.

## 2.2.2 Energy Calibration

Crystal Ball energy calibrations have been carried out by the colleagues from UCLA and Johannes Gutenberg University in Mainz [22]. The energy calibration of the Crystal Ball was performed in three steps; a low energy calibration - mainly important for the acquisition system was obtained, then a high energy calibration has been performed, and in the end, an energy scale factor has been applied to account for crystal thresholds and clustering algorithms.

### 2.2.2.1 Low energy calibration

In this first step of the CB energy calibration, an  $^{241}\text{Am}/^9\text{Be}$  source was placed in the centre of the Crystal Ball [22]. The  $\alpha$  decay of americium, and a subsequent capture of these particles by beryllium, triggers a series of reactions resulting in the excited state of  $^{12}\text{C}$  which decays to a ground state and emits a 4.438 MeV photon in the process. This photon energy deposit in the NaI crystals has been used to adjust the gains of all PMTs, so that the detected peak was in the same position in the ADC spectra for all the detector elements.

### 2.2.2.2 High energy calibration

The photons produced in meson decay have energies much higher than photons used in the low energy calibration, therefore the calibration for higher energy photons is also required. The  $\pi^0 \rightarrow \gamma\gamma$  reaction has been used as a source of such photons. The invariant mass,  $M_{\gamma\gamma}$ , of two photons detected in the CB was reconstructed from the information on the photons measured energy and

momentum and only the events with  $M_{\gamma\gamma}$  within the mass of  $\pi^0$  were selected, and the following selection cuts have been applied:

- no less than 70% of the detected photon energy had to be deposited in a single NaI crystal. This criterium was decided upon to ensure the deposit in a single crystal dominated the cluster.
- in order to ensure that the photons used for the calibration were of similar energy, the condition of having the energy difference between two photon clusters being less than 35% of the total energy have been set up.
- the tagged photon energy had to be less than 180MeV. This restriction constrained the energy range of the decay photons between 40MeV and 125MeV. Such energy cut favoured large opening angles between the photons, resulting in an even angular distributions in the lab.

The invariant mass of  $\pi^0$  has been reconstructed from the two photon decay, and a Gaussian function has been fitted. The mean of the fit, corresponding to  $M_{\gamma\gamma}$ , has been compared to the mass of  $\pi^0$ . With this information a new gain factor,  $G_{new}$ , was obtained according to the below equation:

$$G_{new} = \frac{M_{\gamma\gamma}}{M_{\pi^0}} G_{old} \left[ \frac{MeV}{channel} \right] \quad (2.3)$$

where,  $G_{old}$  is the gain factor used previously. Because the detected energy of the photon cluster depended both, on the central crystal and all the other crystals in the cluster a single set of calculation to obtain the new gain was not enough. Several iterations were required for  $M_{\gamma\gamma}$  to correspond to  $M_{\pi^0}$ .

### 2.2.2.3 Energy scaling factor

Because of the energy losses due to individual energy thresholds and the showers, the energy of the incident photons is not the same as the total energy of the cluster. To account for this in the analysis, another energy correction had to be applied. In order to ensure that the mass reconstructed from the decay of two photons was indeed the mass of  $\pi^0$  meson, a scaling factor of 1.05 was applied to the data.

### 2.2.2.4 Time walk correction

Because of the slow time response of the NaI crystals, 250ns [14], there arises a time difference between the small and large signals registering at the discriminator threshold. Therefore, the times reported by the TDCs required a correction to account for this time difference and therefore improve the CB time resolution (Fig. 2.2). The corrected time,  $T_{corr}$ , is defined as:

$$T_{corr} = T - r \sqrt{\frac{a_0}{a}} \quad (2.4)$$

where,  $T$  is the measured time,  $a_0$  is the discriminator's voltage,  $r$  is the rise time and  $a$  is the signal's amplitude.

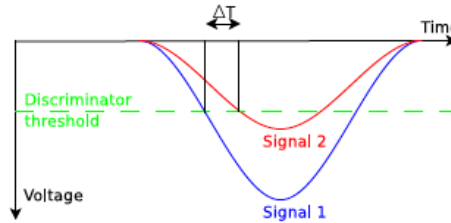


Figure 2.2: CB time walk.

## 2.3 PID Calibration

### 2.3.1 PID azimuthal correction

In order to accurately determine the correlation between hits in the PID and Crystal Ball, the PID azimuthal angle ( $\phi$ ) with respect to the Crystal Ball had to be measured. The steps taken to calculate the value of phi are as follows.

First, only the events that triggered signal in one crystal in a CB cluster were selected. The reason for that was to limit the number of photons producing events in more than one crystal and therefore, ensure that only events with clearly determined angles were considered for the calibration. Another cut was made on those events to select only those with just a single reaction in the PID. This way the background due to multi-body final state interactions was highly

reduced. The angular distribution of those events has been plotted for each PID element, which gave a single peak over the azimuthal range of each one (Fig. 2.3). A 1D projection has been plotted for each PID element and a Gaussian function was fitted to the peak. Having 24 PID elements means that each of them occupies 15deg of the total azimuthal coverage. Therefore, a linear fit with a fixed gradient could have been used to accurately determine the PID azimuthal correction (Fig. 2.4).

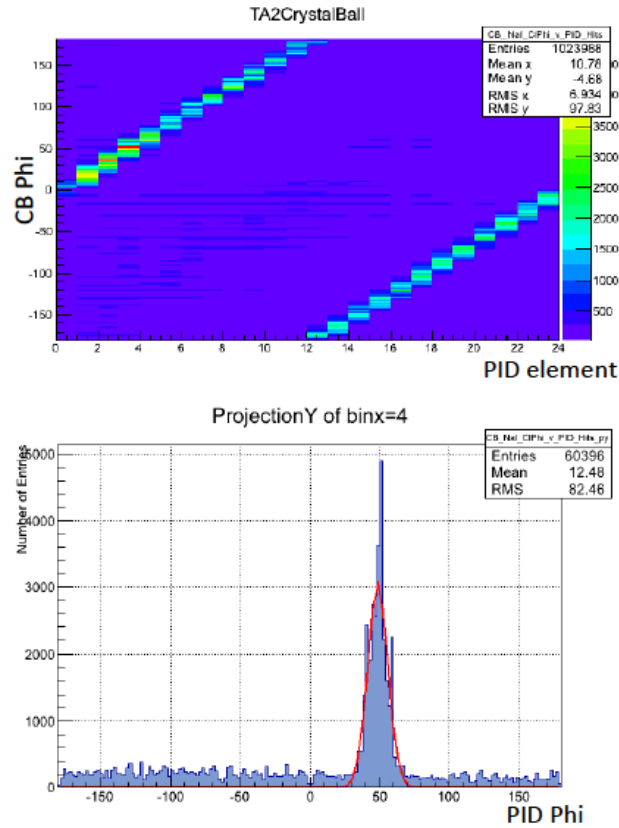


Figure 2.3: Plot of Phi position in CB cluster vs hit in PID (top) and Gaussian fit to the projection of PID element 4 over the azimuthal range (bottom).

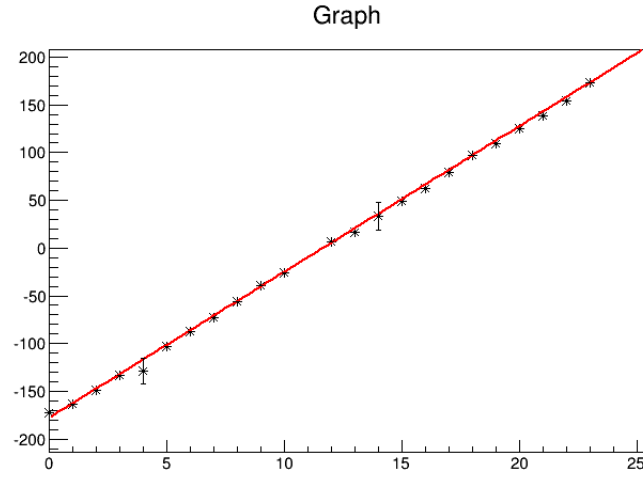


Figure 2.4: PID azimuthal correction - linear fit.

### 2.3.2 PID energy correction

The energy calibration employed banana ( $\Delta E$ - $E$ ) plots described earlier and raw signal from PID ADCs. The banana plots were divided into 10MeV energy bins and projected onto the y-axis (Fig. 2.5). Those projections featured two peaks, first one corresponding to the pion and second one representing proton ridges. The latter was fitted with a Gaussian function and the value of the mean has been extracted (Fig. 2.6). This step has been performed for all the energy bins in the range of 20-300MeV. Similarly, the G4 simulated data had the same procedure applied. Subsequently, the means of the Gaussian functions for the experimental data have been plotted against corresponding means for the simulated data and a linear fit has been used to determine the gain for the calibration (Fig. 2.6).

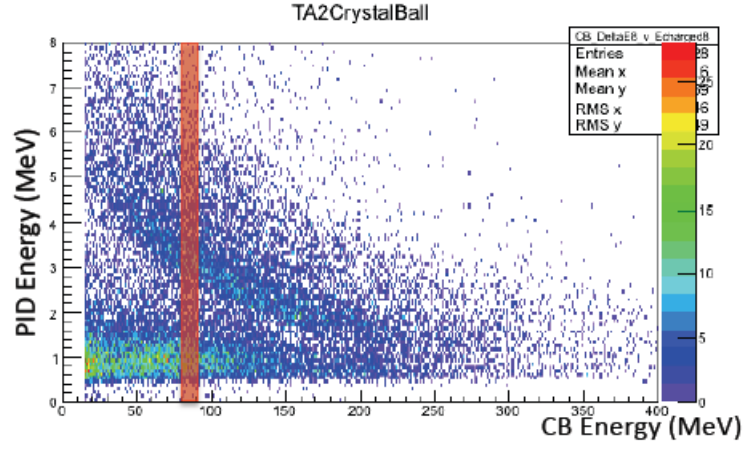


Figure 2.5:  $\Delta E$ -E plots of PID vs CB energy deposits. Example 10 MeV energy bin shaded in red.

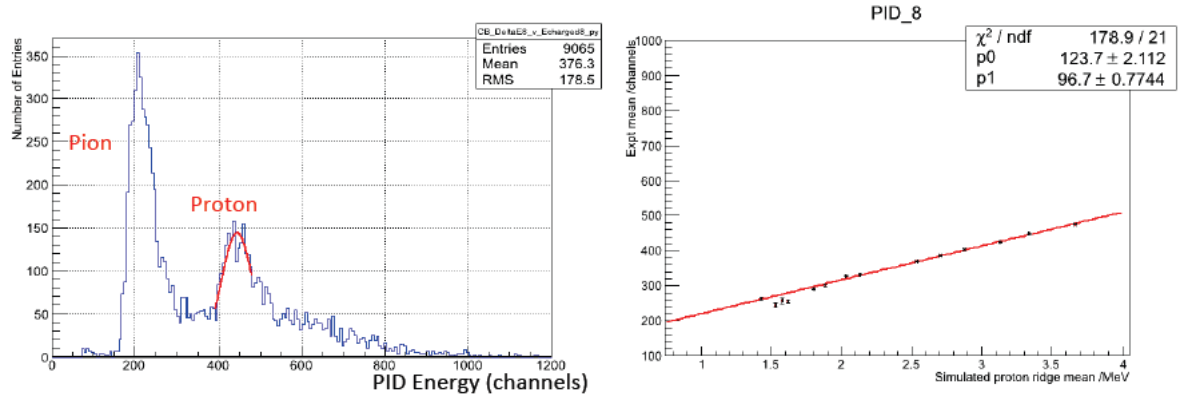


Figure 2.6: Gaussian function fitted to the proton peak (left) and linear fit to the Gaussian means (right).

The offset for the calibration has been obtained from the analysis of the raw ADC signal for each PID element. The first peak in the ADC spectrum (Figure 6) represents the pedestal position. A Gaussian function has been fitted to this peak and the value of the mean has been determined. This value is equivalent to the offset for the calibration.

### 2.3.3 PID time calibration

Accurate information about timing of the events, obtained with the TDCs, is essential part of the data analysis. Timing coincidence allows for correlation of coincidence particles between different detectors; it is used in clustering algorithm of the Crystal Ball, and enables particle identification in TAPS, therefore allowing for the association of a hit in FPD with an even in CB/TAPS detectors. The principles followed for time calibration of the various detectors are the same, therefore, only PID time calibration will be described in more detail below.

The TDC spectrum of each PID element was fitted with a Gaussian and a value of the means for all the elements have been extracted (Fig. 2.7). These values have been used to determine the offset in the calibration and align the peaks of all the detector elements in the timing spectrum (Fig. 2.9). The misalignment for the PID element 17 is caused by the malfunctioning PID element (Fig. 2.8).

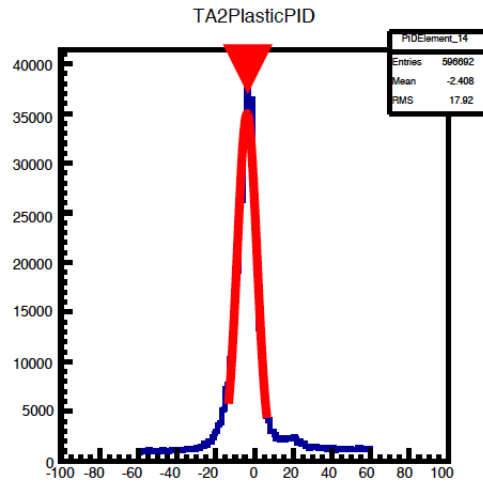


Figure 2.7: Gaussian fit to PID-element 14.

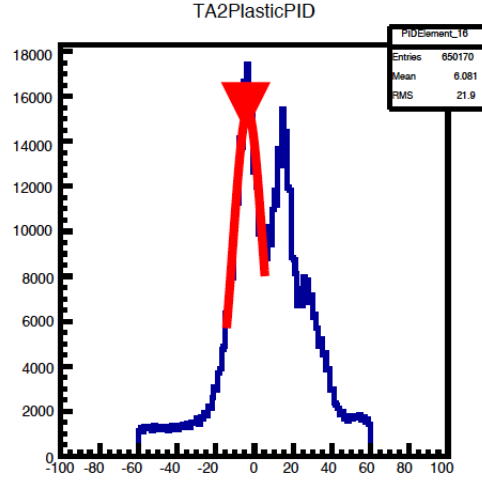


Figure 2.8: Gaussian fit to PID-element 16. The TDC spectrum of the malfunctioning PID element.

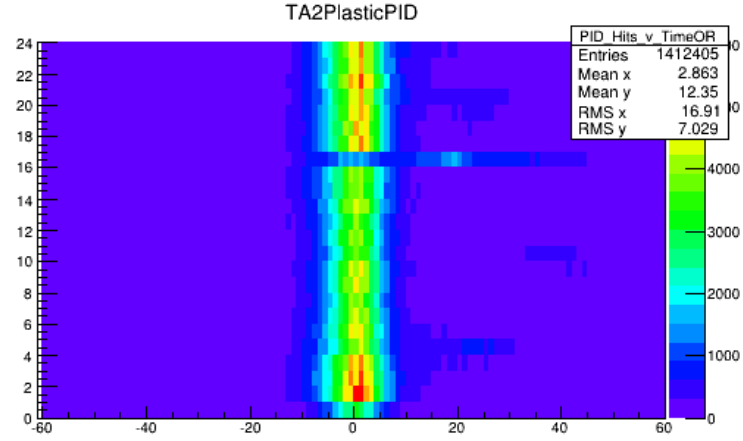


Figure 2.9: Time alignment of all PID elements.

## 2.4 TAPS Calibration

The calibration of the TAPS BaF<sub>2</sub> crystals employed cosmic rays using the mean deposited energy of the minimum ionising muons equal to 37.7MeV [19]. For each of the BaF<sub>2</sub> crystals' PMTs the position of the energy peak has been adjusted



so it was at the same ADC position for all detector elements, and the channel number corresponding to the mean peak position was determined.

Using a similar technique to that employed in the CB calibrations, the correction for the gain was obtained. However, because detection of two photons from the  $\pi^0$  in TAPS is very rare, the events having one photon detected in TAPS and one in CB were chosen. Detailed procedure of this calibration can be found in [16].

The procedure to calibrate plastic Veto was similar to the one used to calibrate PID. The pedestal positions were obtained from the raw ADC spectra and the gain was determined by comparing the experimental mean position of the proton peak in the Veto to the simulated data. Details of this method can be found in reference [11]

## **2.5 Target Position Correction**

# Bibliography

- [1] J. Albert. *Test Measurements for the Crystal Ball Detector at MAMI, PhD thesis*. PhD thesis, 2003.
- [2] J. R. M. Annand. *Data Analysis within an AcqRoot Framework*. *nuclear.gla.ac.uk/acqusys/doc/AcqRoot.11.08.pd*. 2008.
- [3] R. Brun. Root manual [root.cern.ch](http://root.cern.ch), 2015.
- [4] M. Dehn and et al. *Eur. Phys. J. Special Topics* 198, page 1947, 2011.
- [5] A. Starostin et al. *Phys.Rev.C* 64, pages 55–205, 2001.
- [6] Audit et al. *Nuc. Inst. Meth. A* 301, pages 473–481, 1991.
- [7] G. Bruan et al. Tdc chip and readout driver developments for compass and lhc experiments. *arXiv:hep-ex*, 1998.
- [8] Lie-Wen Chen et al. *Proceedings of the 13th National Conference on Nuclear Structure in China*. 2011.
- [9] M. Centelles et al. *Phys Rev Let.* 102, pages 122–502, 2009.
- [10] M. Oreglia et al. *Phys. Rev. D.* 25, page 9, 1982.
- [11] T. Gesslerr. *Bachelor thesis*. Universitaet, Giessen, 2008.
- [12] S.J. Hall, G.J. Miller, R. Beck, and P. Jennewein. *Nucl. Instrum. Methods A* 368, page 698, 1996.
- [13] et al. J C. McGeorge, J. D. Kellie. *Eur. Phys. J. A*, 37, pages 129–137, 2008.
- [14] G.F. Knoll. *Radiation Detection and Measurement*. John Wiley and Sons.
- [15] D. Krambrich. *University of Mainz, PhD thesis*. PhD thesis.
- [16] B. Lemmer. *Diploma thesis*. Universitaet, Giessen, 2007.
- [17] D. Middleton. *Mainz a2 tagger calibrations a2 internal report.*, 2011.
- [18] R. Novotny. *IEEE Trans. Nucl. Sci.* 38, page 2, 1991.
- [19] M. E. Roebig. *Diploma thesis*. Universitaet Giessen, 1991.

- [20] L. Schmitt. *IEEE Trans.Nucl.Sci.*, pages 51:438–444, 2004.
- [21] C. M. Tarbet. *Coherent  $\pi^0$  photoproduction on nuclei*. University of Edinburgh, 2007.
- [22] M. Unverzagt. *Diploma thesis*. University of Mainz, 2004.
- [23] M. Unverzagt. *Nucl.Phys.Proc.Suppl. 198*, pages 174–181, 2010.
- [24] A2 MAMI website. <http://wwwa2.kph.uni-mainz.de>, 2015.